Spaceborne Staring Spotlight SAR Tomography—A First Demonstration With TerraSAR-X

Nan Ge, Fernando Rodriguez Gonzalez, Yuanyuan Wang, *Member, IEEE*, Yilei Shi, *Member, IEEE*, and Xiao Xiang Zhu, *Senior Member, IEEE*

***Abstract*—With the objective of exploiting hardware capabilities and preparing the ground for the next-generation X-band synthetic aperture radar (SAR) missions, TerraSAR-X and TanDEM-X are now able to operate in staring spotlight mode, which is characterized by an increased azimuth resolution of approximately 0.24 m compared with 1.1 m of the conventional sliding spotlight mode. In this paper, we demonstrate for the first time its potential for SAR tomography (TomoSAR). To this end, we tailored our interferometric and tomographic processors for the distinctive features of the staring spotlight mode, which will be analyzed accordingly. By means of its higher spatial resolution, the staring spotlight mode will not only lead to a denser point cloud but also to more accurate height estimates due to the higher signal-to-clutter ratio. As a result of a first comparison between sliding and staring spotlight TomoSAR, first, the density of the *staring* spotlight point cloud is approximately 5.1–5.5 times as high; and, second, the relative height accuracy of the *staring* spotlight point cloud is approximately 1.7 times as high.**

***Index Terms*—SAR tomography (TomoSAR), staring spotlight, synthetic aperture radar (SAR), TerraSAR-X.**

I. Introduction

TERRASAR-X and TanDEM-X, the twin German satellites of an almost identical build, have been delivering high-resolution X-band synthetic aperture radar (SAR) images since their launch in 2007 and 2010, respectively. Among civil SAR satellites, their unprecedented high spatial resolution in meter range and relatively short revisit time of 11 days opened up new applications of spaceborne SAR interferometry (InSAR). As a benchmark of medium-resolution spaceborne SAR sensors, a resolution cell in an ENVISAT ASAR stripmap product of the size 6×9 m^2 (azimuth-by-range) is resolved by approximately 5×15 pixels in a high-resolution sliding spotlight image of TerraSAR-X with 300-MHz range bandwidth [1]. Particularly in urban areas, this meter-level resolution provides the possibility of revealing detailed information in terms of the geolocation and motion of single man-made objects. Adaptations of advanced time-series analysis methods, such as persistent scatterer interferometry (PSI) and SAR tomography (TomoSAR), to sliding spotlight datasets showed promising results (see, for example, [2]–[5]).

In order to fully exploit the capabilities of TerraSAR-X[1] and to prepare for the next-generation X-band SAR satellite missions, e.g., HRWS [6], the TerraSAR-X staring spotlight mode was conceptualized and consequently operationalized [7], [8]. Compared with the high-resolution sliding spotlight mode, the SAR sensor in staring spotlight mode employs a larger squint angle range to achieve a better azimuth resolution of approximately 0.24 m. As a result, the same ENVISAT ASAR stripmap pixel, as mentioned in the previous paragraph, is represented by 25×15 pixels in a staring spotlight image. The advantages of increased (azimuth) resolution for urban areas are at least two-fold.

1) It is more likely for pointlike targets with similar azimuth–range coordinates to appear in different resolution cells, thus densifying the four-dimensional (4-D) point cloud.
2) Pointlike targets stand out more prominently from a clutter, which leads to higher signal-to-clutter ratio (SCR).

These factors favor PSI and TomoSAR in different ways. While the former increases the amount of information of particularly single man-made objects, the latter provides a better lower bound on the variance of height estimates [9].

Although it seems encouraging to adapt and apply TomoSAR to staring spotlight datasets, yet, to the best of our knowledge, there has not been any published result. A lack of datasets could be one reason. On the other hand, several considerations regarding staring spotlight mode need to be taken into account during InSAR processing, which might also hinder such an application. Through this paper, we intend to show that staring

Manuscript received September 8, 2017; revised January 18, 2018 and May 15, 2018; accepted June 14, 2018. Date of publication August 13, 2018; date of current version October 15, 2018. This work was supported in part by Helmholtz Association under the framework of the Young Investigators Group "SiPEO" under Grant VH-NG-1018 and in part by the European Research Council (ERC) through the European Union's Horizon 2020 research and innovation program under Grant ERC-2016-StG-714087 (So2Sat) in part by Munich Aerospace e.V. Fakultät für Luft- und Raumfahrt, and in part by the Bavarian Academy of Sciences and Humanities in the framework of Junges Kolleg. *(Corresponding author: Xiao Xiang Zhu.)*

N. Ge and F. R. Gonzalez are with the Remote Sensing Technology Institute, German Aerospace Center (DLR), 82234 Wessling, Germany (e-mail: Nan.Ge@dlr.de; Fernando.RodriguezGonzalez@dlr.de).

Y.-Y. Wang is with the Signal Processing in Earth Observation, Technical University of Munich, 80333 Munich, Germany (e-mail: wang@bv.tum.de).

Y. Shi is with the Remote Sensing Technology, Technical University of Munich, 80333 Munich, Germany (e-mail: yilei.shi@tum.de).

X. X. Zhu is with the Remote Sensing Technology Institute, German Aerospace Center (DLR), 82234 Wessling, Germany, and also with Signal Processing in Earth Observation,Technical University of Munich, 80333 Munich, Germany (e-mail: xiao.zhu@dlr.de).

Color versions of one or more of the figures in this paper are available online at http://ieeexplore.ieee.org.

Digital Object Identifier 10.1109/JSTARS.2018.2851752

[1]In the following, TerraSAR-X is referred to as the monostatic constellation of TerraSAR-X and TanDEM-X, i.e., the SAR instrument is activated on either TerraSAR-X or TanDEM-X but not both.

1939-1404 © 2018 IEEE. Personal use is permitted, but republication/redistribution requires IEEE permission.
See http://www.ieee.org/publications_standards/publications/rights/index.html for more information.

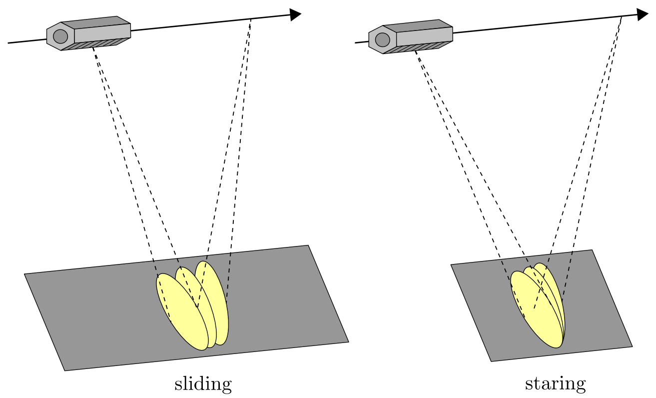

Fig. 1. TerraSAR-X sliding (left) and staring (right) spotlight imaging geometries. Modified from [1].

spotlight datasets are indeed suitable for TomoSAR. Based on a sufficient number of acquisitions, our first results on the scales of a city and of individual infrastructures are demonstrated to provide an argument in favor of this statement. We also perform a preliminary comparison between sliding and staring spotlight TomoSAR by using a limited number of datasets in both modes.

The remainder of this paper is organized as follows. Section II explains the TerraSAR-X staring spotlight mode and its related InSAR processing aspects. The principles of TomoSAR are briefly revisited in Section III, where several technical adaptations are elucidated as well. Section IV comprises our first results with an interferometric stack of Washington, DC, USA, and some interpretations thereof. In Section V, a preliminary comparison of sliding and staring spotlight TomoSAR is made based on a small number of images. Conclusions are drawn and future work is proposed in Section VI. The Appendix clarifies the structure of the TerraSAR-X annotation component containing a 3×3 grid of Doppler centroid in focused image time, which could be used to avoid complex time conversions.

II. TerraSAR-X Staring Spotlight Interferometry

In the spotlight mode, the SAR sensor steers the azimuth beam forth and back in order to increase the illumination (or aperture) time t_{AP} of a target, as illustrated in Fig. 1. As a side effect, the Doppler centroid frequency undergoes a negative drift in azimuth time t_{az} of the raw data (see Fig. 2). The beam sweep rate is a tradeoff between the azimuth resolution and spatial extent. In the TerraSAR-X sliding spotlight mode, the azimuth beam is swept at a moderate rate with a squint angle range of up to $\pm 0.75^\circ$ [10], while in the staring spotlight mode the azimuth beam is steered exactly towards a reference ground target as the satellite proceeds. In other words, the beam sweep rate is configured to match the frequency modulation (FM) rate of the reference target, which enables a longer azimuth illumination time. To be more specific, the acquisition squint angle range is restricted to approximately $\pm 2.2^\circ$ due to the antenna azimuth grating lobe [7]. As a consequence, t_{AP} is, in the ideal case, equal to the azimuth time span of the raw data Δt_{raw}. This leads to a maximized azimuth resolution, which is limited by the product of t_{AP} and the FM rate [1]. This improved azimuth resolution comes, however, at the expense of a reduced azimuth

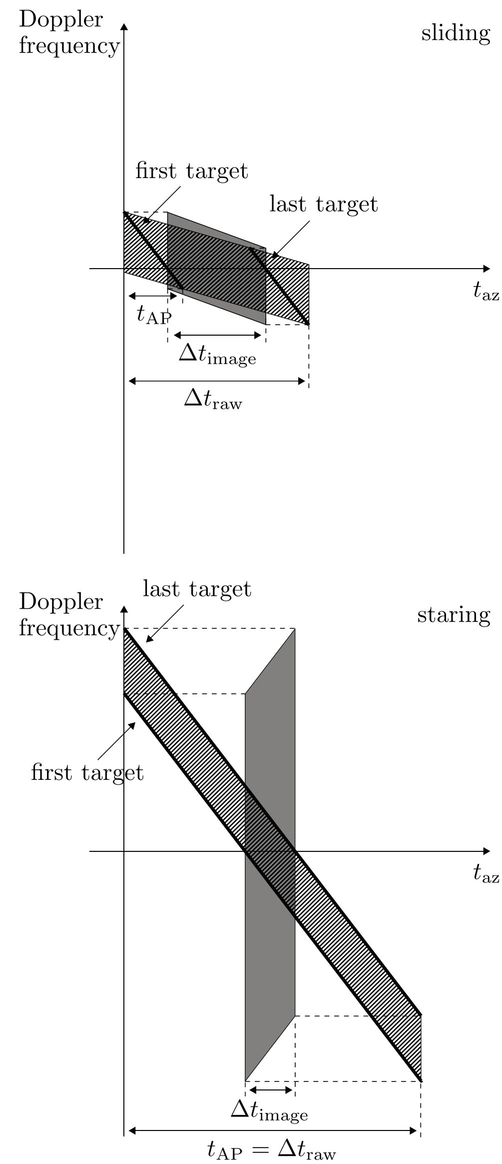

Fig. 2. Time-variant Doppler spectra of SAR raw data (//) with time span Δt_{raw} and of focused image (shaded) with time span $\Delta t_{\mathrm{image}}$ in the sliding (top, modified from [1]) and staring (bottom) spotlight modes. Bold line segments denote the targets at the start and stop azimuth time (t_{az}) in the focused image, respectively. Both targets are illuminated with time t_{AP} and their zero-crossings define $\Delta t_{\mathrm{image}}$. In the staring spotlight mode, t_{AP} is set to equal Δt_{raw} in order to increase the azimuth resolution, which comes at the expense of a significantly shorter $\Delta t_{\mathrm{image}}$.

scene extent, i.e., the azimuth time span of a focused image $\Delta t_{\mathrm{image}}$ in the staring spotlight mode is significantly shorter. Naturally, the intrinsic range bandwidth imposes a ceiling on the slant range resolution, which is normally solely enhanced by a hardware upgrade. Table I lists, as an example, the parameters of a TerraSAR-X staring spotlight acquisition of Washington, DC.

Due to the longer integration time of approximately 7 s in the TerraSAR-X staring spotlight mode, several challenges arise in SAR processing [8], such as the following.

1) The stop-and-go approximation becomes invalid, i.e., satellite movement between transmitting and receiving the chirp signal can no longer be neglected.

TABLE I
EXEMPLARY PARAMETERS OF A TERRASAR-X STARING SPOTLIGHT ACQUISITION OF WASHINGTON, DC (VALUES ARE ROUNDED)

Incidence angle at scene center	41°
Azimuth resolution	0.23 m
Slant range resolution	0.59 m
Azimuth scene extent	3.1 km
Ground Range scene extent	5.5 km
Range bandwidth	300 MHz
Antenna bandwidth	2589 Hz
Focused azimuth bandwidth	38275 Hz
Acquisition pulse repetition frequency (PRF)	4448 Hz
Focused PRF	42300 Hz
Number of azimuth beams	113
Squint angle range	±2.2°
Aperture time t_{AP}	7.24 s
Raw data scene duration Δt_{raw}	7.24 s
Focused scene duration $\Delta t_{\mathrm{image}}$	0.43 s
FM rate at scene center	−5301 Hz/s
Beam sweep rate at scene center	−5301 Hz/s

2) The satellite's trajectory deviates significantly from a linear track, i.e., an orbit curvature needs to be taken into account.
3) The tropospheric delay could vary significantly within the large squint angle span and, therefore, needs to be corrected.

All of these effects are considerately accounted for in a revised version of the TerraSAR-X multimode SAR processor [11], [12].

InSAR processing, on the other hand, requires merely few adaptations. As in the sliding spotlight mode, the master and slave images are co-registered (resampled) on the basis of point-like scatterers in order to generate a coherent interferogram [1]. A requirement is the knowledge of the Doppler centroid frequency f_{DC} as a function of the focused image time t_{image}. Since f_{DC} is annotated as a (first-order) polynomial of the raw data time t_{raw} in the TerraSAR-X products, it is suggested in [1] and [13] to perform a time conversion for the sliding spotlight datasets via the following:

$$t_{\mathrm{image}} = t_{\mathrm{raw}} - \frac{f_{\mathrm{DC}}(t_{\mathrm{raw}})}{\mathrm{FM}}. \quad (1)$$

This relation, however, does not hold for the staring spotlight mode, in which the FM rate equals the beam sweep rate, i.e., a target is visible throughout the whole raw data duration. In order to circumvent this problem, a 3×3 grid containing the f_{DC} in t_{image} is provided as a TerraSAR-X annotation component [13]. Its structure is described in the Appendix of this paper. This grid could be interpolated in order to derive the f_{DC} at every point of the focused image, which allows considering second-order variations of the f_{DC} along a range.

As an example, Fig. 3 shows a differential interferogram of Washington, DC, with an effective baseline of approximately −71 m. The master and slave scenes were acquired on October 31, 2015 and October 9, 2015, respectively, and processed with the integrated wide area processor (IWAP) [14], [15]. A low-pass filtered digital elevation model (DEM) with a spatial resolution of 1 arcsecond from the Shuttle Radar Topography Mission was used. The differential phase consists primarily of a topographic phase that is related to the residual height. As can be seen in Fig. 4, the Theodore Roosevelt Bridge shown in the lower left corner of Fig. 3 is subject to a spatially correlated motion, presumably due to thermal dilation and contraction between piers caused by a periodical temperature change.

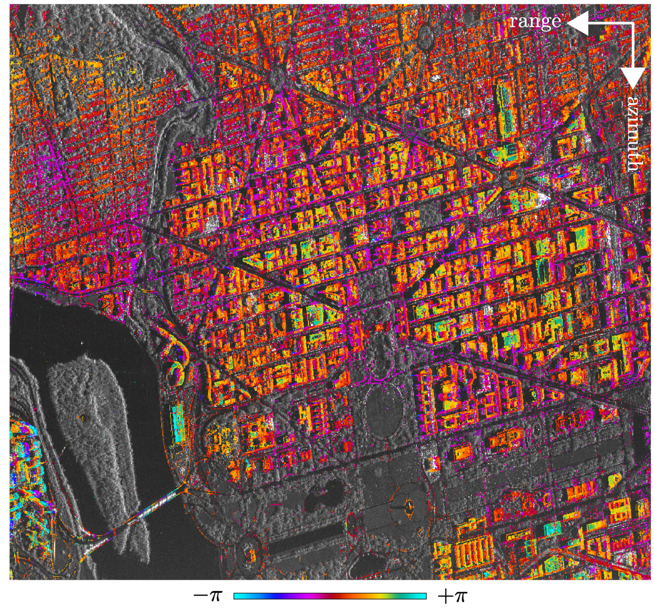

Fig. 3. Staring spotlight differential interferogram of Washington, DC, with a spatial perpendicular baseline of approximately −71 m and a temporal baseline of −22 days.

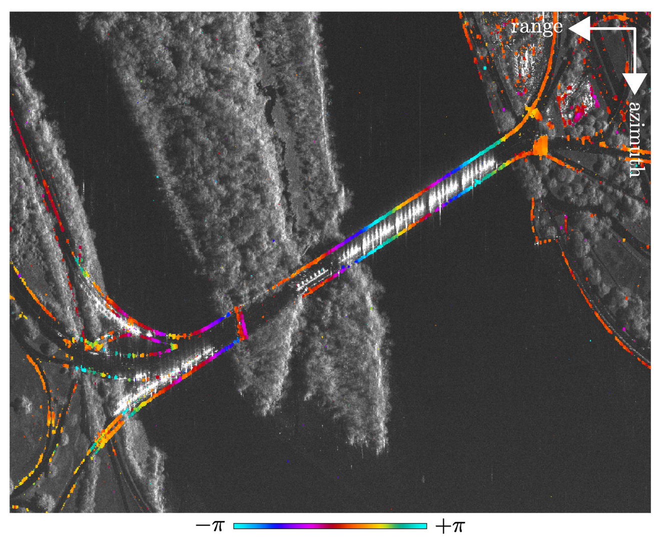

Fig. 4. Zoomed-in view of Fig. 3 on the Theodore Roosevelt Bridge (lower-left).

Section III briefly revisits the principles of TomoSAR and elucidates the processing chain, which was employed to produce the results in Sections IV and V.

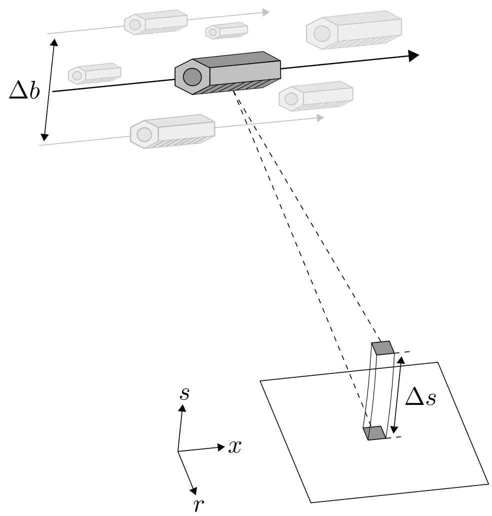

Fig. 5. Layover phenomenon in side-looking SAR imaging. x, r, and s represent the azimuth, range, and elevation axes, respectively, that form a local 3-D Cartesian coordinate system. An elevation aperture Δb is built by means of repeat–pass measurements to resolve multiple scatterers in the far-field toroid segment with elevation extent Δs.

III. TomoSAR Principles

Due to the common side-looking geometry of spaceborne SAR sensors, echoes of the chirp signal from equidistant targets within an elevation extent Δs in the far-field sum to give one measurement for each azimuth–range pixel in the focused image, as illustrated in Fig. 5. The three-dimensional (3-D) azimuth–range–elevation (x–r–s) reflectivity profile is, thus, embedded as two-dimensional (2-D), i.e., information regarding the elevation is encoded during imaging. TomoSAR is a technique to reconstruct the elevation axis from multibaseline measurements [16]–[18]. For a spaceborne SAR, this multibaseline configuration is usually achieved by repeat–pass measurements (depicted as semitransparent satellite models in Fig. 5), in which the scatterers' motion in the course of time often needs to be taken into account. A well-established theory models the complex InSAR measurement g_n of a specific pixel in the nth interferogram as the integration of a phase-modulated elevation-dependent complex reflectivity profile $\gamma(s)$ over Δs [19]–[21], given by

$$g_n \approx \int_{\Delta s} \gamma(s) \exp\big(-i\,2\pi(\xi_n s + 2d(s,t_n)/\lambda)\big)\mathrm{d}s \tag{2}$$

where $\xi_n := 2b_n/(\lambda r)$ is the elevation frequency that is proportional to the effective baseline b_n (λ and r are the radar wavelength and the range between the sensor and target in the master image, respectively) and $d(s,t_n)$ is the line-of-sight displacement of the scatterer at the elevation position s and the temporal baseline t_n. In order to reduce the number of unknowns, $d(s,t_n)$ could be modeled as a linear combination of basis functions. It can be shown that (2) is equivalent to a multidimensional spectral estimation problem [21]. After discretizing s and displacement parameters, and subsequently replacing integration by finite sum, a linear model for all N InSAR measurements can be formulated as follows:

$$\mathbf{g} \approx \mathbf{R}\boldsymbol{\gamma} \tag{3}$$

where $\mathbf{g} := (g_1, \ldots, g_N) \in \mathbb{C}^N$ is the complex InSAR measurement vector, $\mathbf{R} \in \mathbb{C}^{N\times L}$ is the TomoSAR dictionary, and $\boldsymbol{\gamma} \in \mathbb{C}^L$ is the discrete elevation-motion reflectivity profile (or spectrum).

Various algorithms were proposed to estimate $\boldsymbol{\gamma}$ with a given $\mathbf{R}$ and $\mathbf{g}$. A common approach is to use Tikhonov regularization [4] as follows:

$$\underset{\boldsymbol{\gamma}}{\text{minimize}}\ \|\mathbf{R}\boldsymbol{\gamma} - \mathbf{g}\|_2^2 + \delta\|\boldsymbol{\gamma}\|_2^2 \tag{4}$$

where $\delta > 0$ is a regularization constant. Note that (4) is equivalent to the maximum *a posteriori* estimator of $\boldsymbol{\gamma}$, provided that the measurement noise is additive and white with variance δ, and $\boldsymbol{\gamma}$ is white with variance 1.

If one is primarily concerned with man-made objects in high-resolution spotlight images acquired over urban areas, it is deemed reasonable to assume that radar echoes in the far-field are dominated by those from merely few pointlike scatterers within the toroid segment shown in Fig. 5, i.e., $\boldsymbol{\gamma}$ is presumed to be compressible and, thus, $\mathbf{g}$ could be sufficiently approximated by a linear combination of few atoms (columns) of $\mathbf{R}$. This hypothesis gave rise to approaches with sparsity-driven ℓ_1 regularization [22], [23], given by

$$\underset{\boldsymbol{\gamma}}{\text{minimize}}\ \|\mathbf{R}\boldsymbol{\gamma} - \mathbf{g}\|_2^2 + \epsilon\|\boldsymbol{\gamma}\|_1 \tag{5}$$

where $\epsilon > 0$ is another regularization constant.

In terms of the capability to resolve multiple pointlike scatterers, conventional methods, such as Tikhonov regularization (4), are limited by the elevation resolution $\rho_s := \lambda r/(2\Delta b)$, where Δb is the elevation aperture as shown in Fig. 5. For TerraSAR-X, ρ_s is in the order of several tens of meters (typically 20–30 m, given a sufficiently large stack), as a consequence of the satellite being confined to a 250-m orbit tube [24]. Given a single scatterer within the resolution cell, a lower bound on the errors of elevation estimates $\hat{s}$ can be derived [9] as follows:

$$\sigma_{\hat{s}} := \frac{\lambda r}{4\pi\sqrt{N}\sqrt{2\mathrm{SNR}}\,\sigma_b} \tag{6}$$

where SNR is the scatterer's signal-to-noise ratio, and σ_b is the standard deviation of effective baselines. In the case of double scatterers, their mutual interference could be modeled as a scaling factor that depends primarily on their elevation distance and phase difference [25]. For TerraSAR-X, this lower bound is approximately one order smaller than ρ_s and could be approached by means of ℓ_1 regularization (5). In other words, (5) could achieve superresolution [26].

As an overview, a top-down model of the processing chain is illustrated in Fig. 6 and consists primarily of the following parts.

1) *Preprocessing* (via IWAP), which takes focused single-look slant-range complex (SSC) images as the input and performs the following:

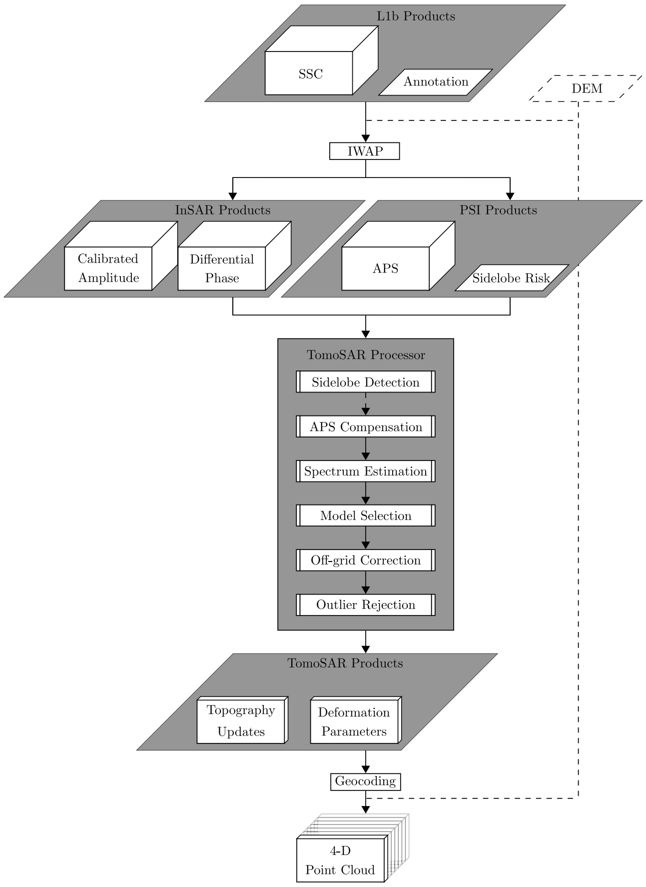

Fig. 6. Top-down model of the processing chain. Modified from [30].

a) *InSAR processing*, which provides raster images of the calibrated amplitude and differential phase; and, subsequently,

b) *PSI processing*, which estimates the atmospheric phase screen (APS) from single pointlike targets and a sidelobe risk map [14], [27], [28].

Note that the use of a DEM is optional if the concerned terrain is relatively flat.

2) *TomoSAR processing.*

a) *Sidelobe detection:* A simple hypothesis test (thresholding) is applied to the sidelobe risk map from 1b).

b) *APS compensation:* The estimated APS is compensated in the differential phase, if the corresponding pixel concerned is, with high probability, not dominated by a sidelobe.

c) *Spectrum estimation:* The elevation-motion spectrum is estimated with, for example, (4) or (5).

d) *Model selection:* By minimizing the penalized negative log-likelihood, the number of scatterers is estimated to reduce the false positive rate [25]. If ℓ_1 regularization is employed in 2c), the underestimated amplitude is, hereby, corrected as a byproduct.

e) *Off-grid correction:* In order to ameliorate the off-grid problem as a consequence of discretizing elevation and motion parameters, the estimated elevation-motion spectrum from 2c) is oversampled in a neighborhood of each statistically significant scatterer. A local maximum is detected in the oversampled high-dimensional signal, which allows a better quantization.

f) *Outlier rejection:* As a natural extension of the complex ensemble coherence for single pointlike scatterers [29], we define the following for the multiple-scatterer case:

$$\eta := \frac{1}{N}\sum_{n=1}^{N} \exp\left(- i \left(\angle \mathbf{r}^n \boldsymbol{\gamma} - \angle g_n \right) \right) \tag{7}$$

where $\angle : \mathbb{C} \rightarrow \mathbb{R}$ returns the phase of a complex number, and $\mathbf{r}^n$ denotes the nth row of the TomoSAR dictionary $\mathbf{R}$. We reject outliers, i.e., scatterers whose phase history deviates significantly from the adopted model, by thresholding of $|\eta|$.

3) *Postprocessing*, which couples the updated topography and its deformation parameters to produce a 4-D geocoded point cloud.

In Section IV, we demonstrate for the first time TerraSAR-X staring spotlight TomoSAR results produced with the abovementioned processing chain. Based on a sufficient number of acquisitions, the demonstration is given not only for individual urban infrastructures but also on the scale of a city.

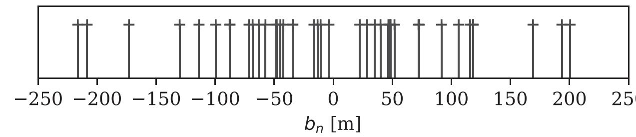

Fig. 7. Distribution of effective baselines b_n.

IV. First Practical Demonstration of Staring Spotlight TomoSAR

Forty-one staring spotlight images were acquired by TerraSAR-X from July 4, 2014 to November 30, 2016 with a constant repeat interval of 22 days, i.e., every second orbit. The image from October 31, 2015 with an incidence angle of 40.7° at the scene center was chosen as the master due to its central position in the spatial–temporal baseline plot and relatively small atmospheric delays. Fig. 7 shows the distribution of effective baselines b_n with respect to the master scene, which are indeed confined to $\pm$250 m. The elevation aperture Δb is approximately 417 m, which leads to an elevation resolution ρ_s of approximately 24.6 m at the scene center. Given an SNR of 2 dB, the lower bound for single pointlike scatterers $\sigma_{\hat{s}}$ is merely 1.44 m, i.e., less than 6% of ρ_s.

As previously mentioned in Section III, the preprocessing (i.e., InSAR and PSI processing) was accomplished by IWAP. In order to decrease the computational cost, we exclusively considered the pixels with SCR ≥ 1.7 dB as candidates for TomoSAR processing, i.e., heavily vegetated areas and water bodies were likely masked out. The number of candidates was further reduced by eliminating those pixels, each of which has

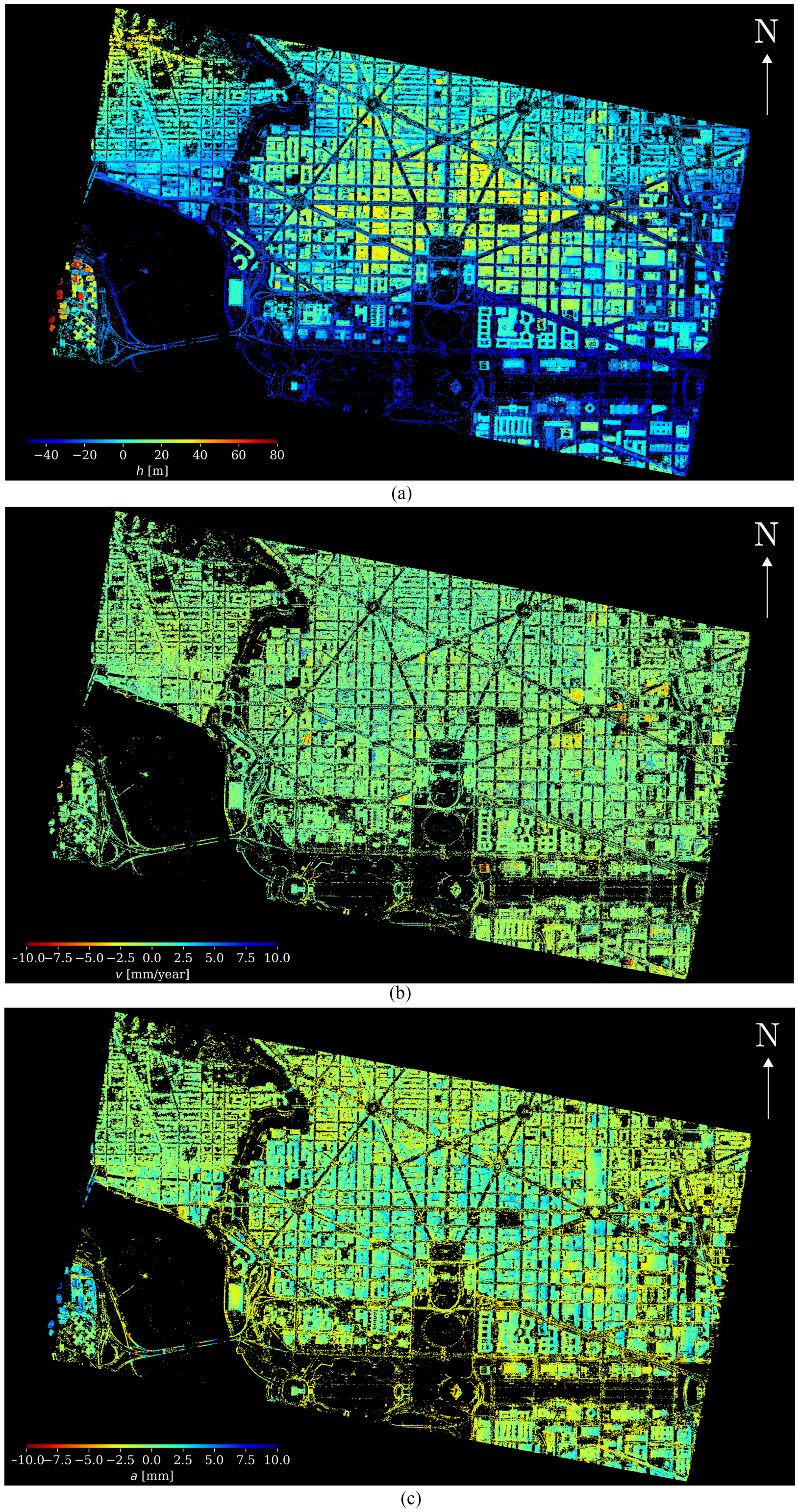

Fig. 8. TomoSAR results of Washington, DC, with 41 TerraSAR-X staring spotlight acquisitions. (a) Updated topography h (m). (b) Linear deformation rate v (mm/year). (c) Periodical deformation amplitude a (mm).

an estimated likelihood of being a sidelobe larger than 0.45. As a result, we only processed approximately 12% of the original raster data. The scatterers' motion was modeled with a coupled linear model and a sinusoidal model with the latter having a period of one year. The elevation-motion spectrum was estimated either with Tikhonov regularization (4) for the whole scene or with ℓ_1 regularization (5) for certain regions of interest. The maximum number of pointlike scatterers within each

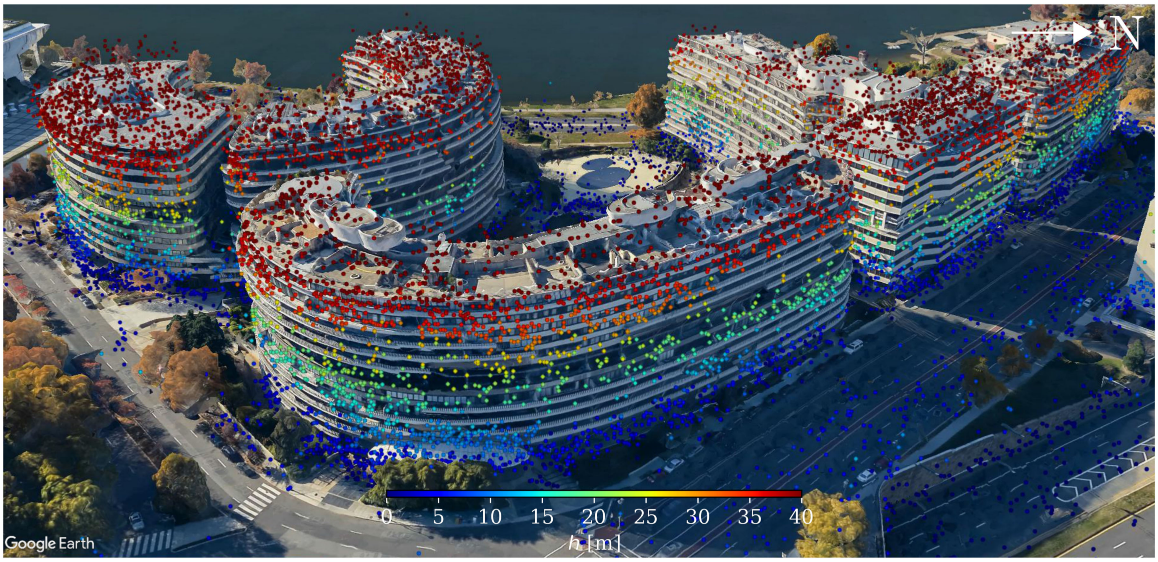

Fig. 9. Original point cloud (6%) of the Watergate complex that is overlaid on Google Earth 3-D photo-realistic building model and color-coded by the updated topography h (m).

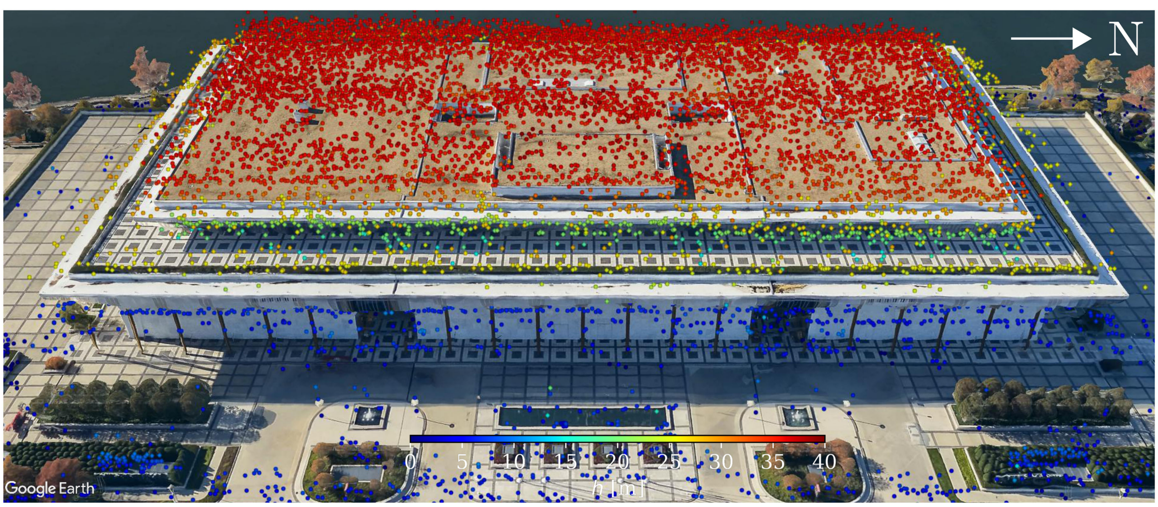

Fig. 10. Original point cloud (6%) of the John F. Kennedy Center for the Performing Arts that is overlaid on Google Earth 3-D photo-realistic building model and color-coded by the updated topography h (m).

resolution cell was set to 2, and the model selector was trained such that the false positive rate for double scatterers, i.e., the empirical probability that two scatterers are detected whereas there is at most one, is below 0.1%. A neighborhood of each selected scatterer in its 3-D elevation-motion (s–v–a, where v is the linear deformation rate and a is the periodical deformation amplitude) spectrum was oversampled with a factor of 10 to alleviate the off-grid problem. Scatterers with an ensemble coherence (7) less than 0.6 were considered as outliers and excluded from postprocessing.

The updated topography h, the linear deformation rate v, and the periodical deformation amplitude a are shown in Fig. 8(a)–(c), respectively. On the Potomac River (lower left), scarcely any pointlike scatterers could be detected, except for those from the National Memorial on the Theodore Roosevelt Island (see Fig. 3) and those on the Theodore Roosevelt Bridge (see Fig. 4). The National Mall in the lower part is in general void of pointlike scatterers due to its vegetation.

Most of the buildings in the scene appear to be flat with the exception of several high-rise ones in Rosslyn, VA, USA (lower left, to the west of the Theodore Roosevelt Bridge). Zoomed-in views of the Watergate complex and the John F. Kennedy Center for the Performing Arts are shown in Figs. 9 and 10, respectively. Due to the limitations of Google Earth, merely 6% of the original point cloud was used for visualization.

Bridges and overpasses are in general subject to periodical deformation as a result of temperature changes, i.e., dilation between piers or fixed bearings in summer and contraction in winter. The estimated periodical deformation amplitude of the Theodore Roosevelt Bridge is shown in Fig. 11. As an example, Fig. 12 depicts the phase history of two scatterers within a resolution cell. The higher scatterer (depicted as a red dot) is

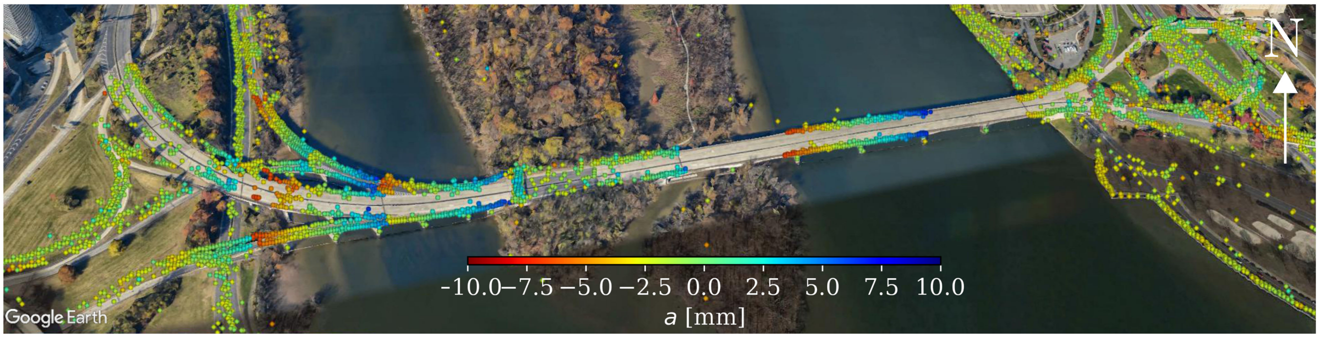

Fig. 11. Original point cloud (6%) of the Theodore Roosevelt Bridge that is overlaid on Google Earth 3-D photo-realistic building model and color-coded by the periodical deformation amplitude a (mm).

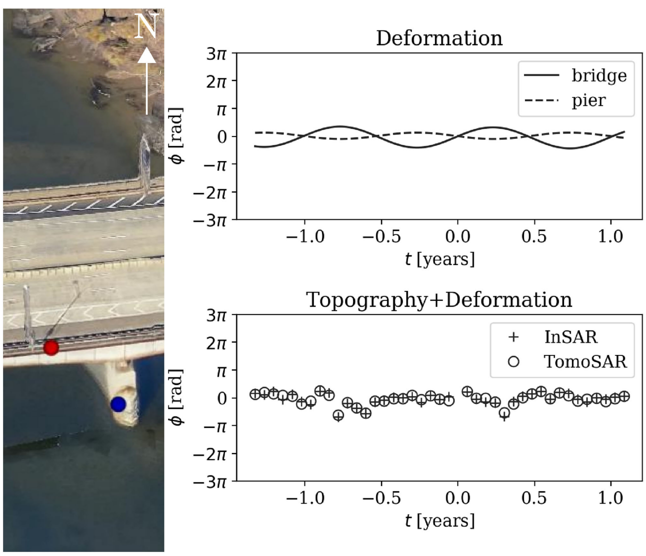

Fig. 12. Phase history of InSAR measurements and TomoSAR reconstruction of double scatterers subject to the layover in Fig. 11. The higher and lower scatterers are marked as red and blue, respectively.

located on the bridge, while the lower (blue) resides at one of the piers. The estimated height difference of these two scatterers is approximately 8.3 m, which lies in the superresolution regime. As the upper-right plot of Fig. 12 depicts, the lower scatterer on the pier undergoes little deformation, whereas the periodical deformation amplitude of the higher scatterer on the bridge was estimated to be approximately 2.9 mm. The topography and deformation model of double scatterers fits quite well with the InSAR measurements (see the lower-right plot of Fig. 12), and the ensemble coherence amounts to approximately 0.97.

The Washington Marriott Marquis hotel (opened on May 1, 2014) beside the Walter E. Washington Convention Center appears to suffer from subsidence that is presumably due to the building weight [see Fig. 13(a)]. In addition, it undergoes thermal dilation and contraction that are more significant on the roof than on the facade, as can be seen in Fig. 13(b). Fig. 14 shows the resolved layover effect of two scatterers, which is a typical case of roof–facade interaction. The higher and lower scatterers subside at a linear rate of −1.1 and −1.0 mm/year, respectively. The scatterer on the roof moves periodically with an amplitude of approximately 3.0 mm, while, on the contrary, the one on the facade is subject to little such deformation. Similar to the previous example depicted in Fig. 12, the TomoSAR model could describe the phase history sufficiently well with an ensemble coherence of approximately 0.97.

As one last example, Fig. 15(a) and (b) shows the updated topography and periodical deformation amplitude of the Rosslyn Twin Towers, respectively. Clearly, the amplitude of thermal dilation and contraction is highly correlated with the building height. Note that the tower on the left has a smaller point density on the left-hand side of the facade due to its convex shape, as seen from the radar wavefront. Fig. 16 depicts another typical case of layover effect in urban areas, which is the facade–ground (or facade–lower-infrastructure) interaction. The periodical deformation amplitude of the higher and lower scatterers was estimated to be approximately 5.0 and 2.0 mm, respectively.

Section V reports a preliminary comparison of the sliding and staring spotlight TomoSAR using TerraSAR-X data. The comparison is based on a limited number of acquisitions and, therefore, restricted to two small typical urban areas.

V. Preliminary Comparison of Sliding and Staring Spotlight TomoSAR

Due to data unavailability, a direct comparative study of both modes was not possible for Washington DC. Instead, we drew the comparison with two small descending interferometric stacks of the City of Las Vegas. Each stack contains 12 images, which were acquired alternately from October, 2014 to February, 2015 during the TanDEM-X Science Phase [31]. For each mode, 11 interferograms were generated with a similar baseline distribution as shown in Fig. 7.

Two small areas were selected for the comparison of the sliding and staring spotlight TomoSAR. One of them is a relatively flat area of approximately 0.01 km^2. The same area of interest was cropped in both datasets using ground control points. Fig. 17 shows the mean intensity map in each mode. In the staring spotlight case, pointlike targets appear more focused, which indicates an increase of the SCR. As a result, the contrast between areas of different degrees of smoothness becomes larger, i.e., the boundaries of the rectangular surfaces in the middle of the image are much easier to recognize. The reconstructed TomoSAR point cloud is shown in Fig. 18. An increase

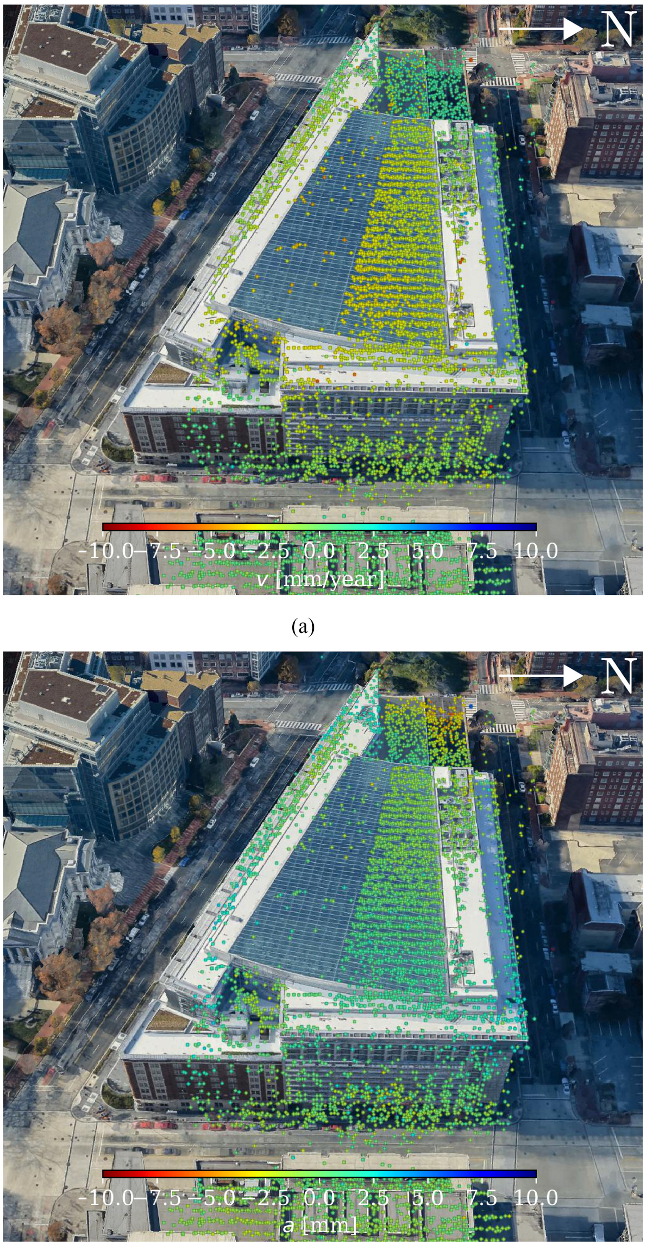

(a)

(b)

Fig. 13. Original point cloud (4%) of the Washington Marriott Marquis hotel that is overlaid on Google Earth 3-D photo-realistic building model. (a) Linear deformation rate v (mm/year). (b) Periodical deformation amplitude a (mm).

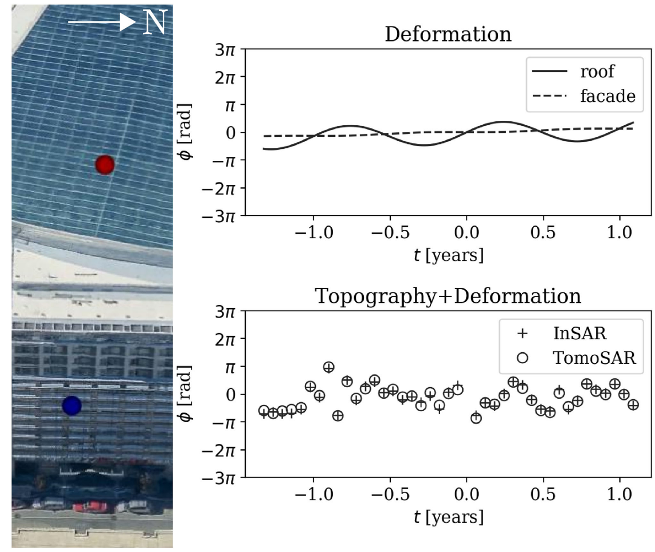

Fig. 14. Phase history of InSAR measurements and TomoSAR reconstruction of double scatterers subject to the layover in Fig. 13. The higher and lower scatterers are marked as red and blue, respectively.

in the number of points in the staring spotlight mode is obvious. Indeed, the point density in the staring spotlight case is approximately 5.5 times as high (see Table II).

The assessment of the relative height accuracy is explained as follows. Since this area is relatively flat (see Fig. 18), we fitted a plane with robust measure through each point cloud and considered it as a partial ground truth. Note that this also took the local slope into account. Subsequently, we calculated the distance of each scatterer to the fitted plane and projected it into the vertical direction. In this context, we refer to the median absolute deviation of height estimate errors relative to this fitted plane as the relative height accuracy.

Let us denote the vectors containing the geographic coordinates of all m scatterers as $\tilde{\mathbf{x}}, \tilde{\mathbf{y}}, \tilde{\mathbf{z}} \in \mathbb{R}^m$. We seek a plane parameterized by $\tilde{a}, \tilde{b}, \tilde{c}, \tilde{d} \in \mathbb{R}$ such that

$$\tilde{a}\tilde{x} + \tilde{b}\tilde{y} + \tilde{c}\tilde{z} + \tilde{d} \approx 0 \tag{8}$$

for each scatterer at the coordinates $\tilde{x} \in \tilde{\mathbf{x}}$, $\tilde{y} \in \tilde{\mathbf{y}}$, and $\tilde{z} \in \tilde{\mathbf{z}}$. Without loss of generality, let us assume that $\tilde{c} = 1$. The plane-fitting problem can be formulated as follows:

$$\underset{\mathbf{x}}{\text{minimize}} \, \|\mathbf{A}\mathbf{x} - \mathbf{b}\|_1 \tag{9}$$

where $\mathbf{A} := \begin{pmatrix} \tilde{\mathbf{x}} & \tilde{\mathbf{y}} & \mathbf{1} \end{pmatrix} \in \mathbb{R}^{m \times 3}$, $\mathbf{1}$ is an m-dimensional vector of ones, $\mathbf{x} := \begin{pmatrix} \tilde{a} & \tilde{b} & \tilde{d} \end{pmatrix}^{\mathrm{T}} \in \mathbb{R}^3$, and $\mathbf{b} - \tilde{\mathbf{z}}$. The ℓ_1 loss function is known for its robustness against outliers [32]. Let $\mathbf{x}^*$ denote an optimal solution and $\mathbf{n} := \begin{pmatrix} x_1^* & x_2^* & 1 \end{pmatrix}^{\mathrm{T}}$ be a corresponding plane normal. The signed distance of scatterers to the fitted plane is given by $(\mathbf{A}\mathbf{x}^* + \tilde{\mathbf{z}})/\|\mathbf{n}\|_2$. Due to the large scale of problem (9), i.e., $m > 10^5$ as presented in Table II, generic conic solvers may not be able to solve it efficiently. Based on the alternating direction method of multipliers (ADMM) [33], we developed a fast solver with a superlinear convergence rate (see Algorithm 1), where $\mathbf{z}$ and $\mathbf{y}$ are auxiliary primal and dual variables, respectively, $\rho > 0$ is a penalty parameter for a smoothness term in the augmented Lagrangian (fixed to 1 in this paper), and $\mathrm{prox}_{\ell_1,\lambda}(\mathbf{w}) := (\mathbf{w} - \lambda)_+ - (-\mathbf{w} - \lambda)_+$ is the element-wise soft thresholding operator [34], where $(\mathbf{u})_+ := \max(\mathbf{u}, 0)$ replaces the negative entries with zeros.

Fig. 19 depicts the errors of height estimates relative to the fitted plane. Although both normalized histograms are centered around zero, the height estimate errors in the staring spotlight mode exhibit less deviation. According to Table III, the relative height accuracy (defined as the median absolute deviation of height estimate errors) in the sliding spotlight case is approximately 1.7 times as high.

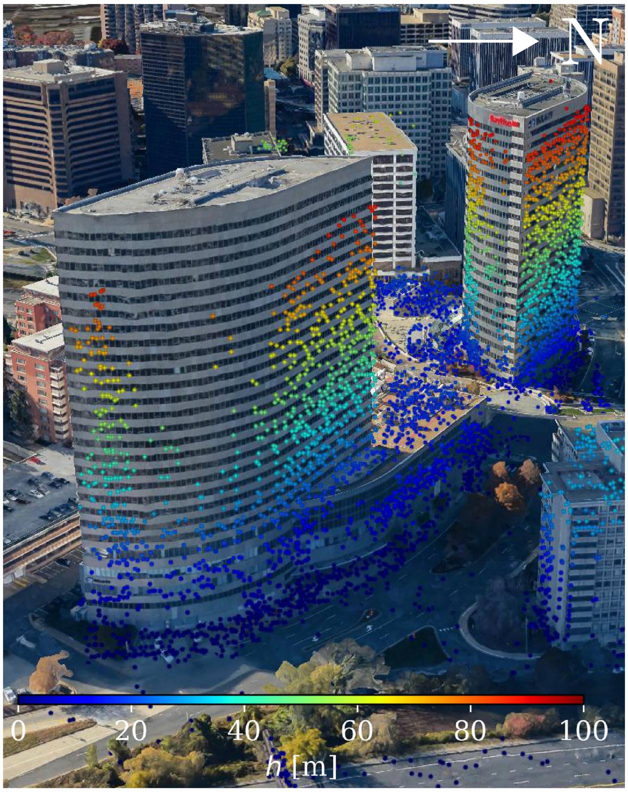

(a)

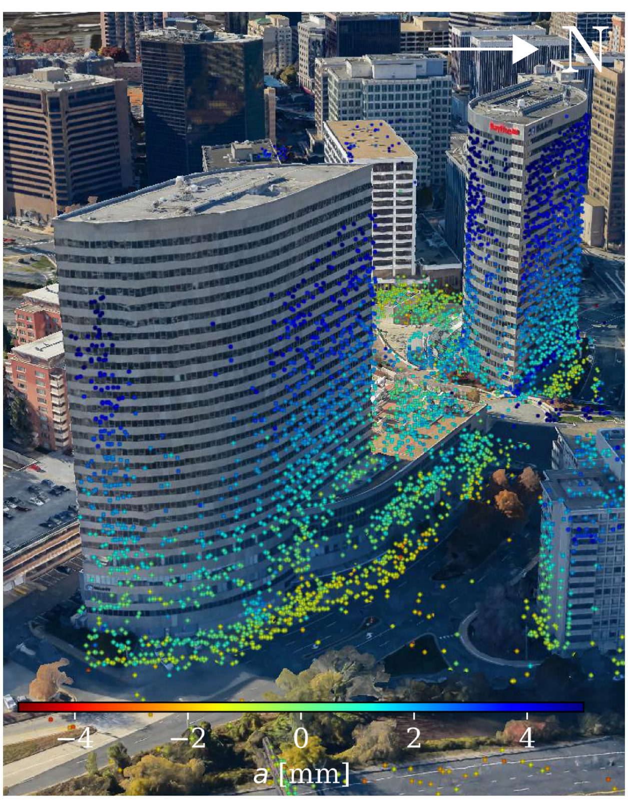

(b)

Fig. 15. Original point cloud (5%) of the Rosslyn Twin Towers that is overlaid on Google Earth 3-D photo-realistic building model. (a) Updated topography h (m). (b) Periodical deformation amplitude a (mm).

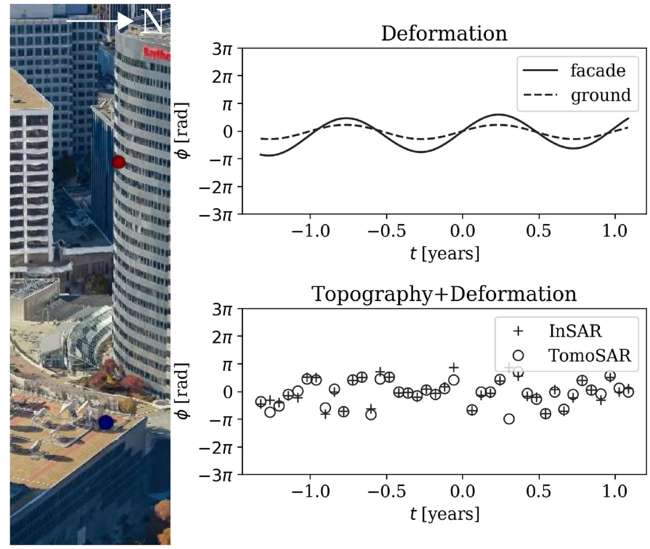

Fig. 16. Phase history of InSAR measurements and TomoSAR reconstruction of double scatterers subject to the layover in Fig. 15. The higher and lower scatterers are marked as red and blue, respectively.

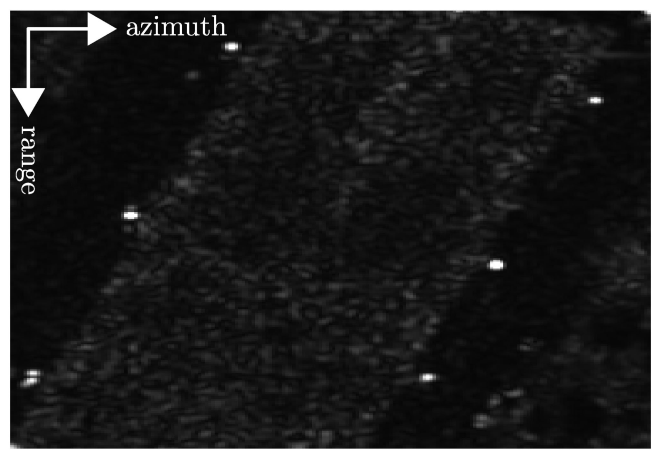

(a)

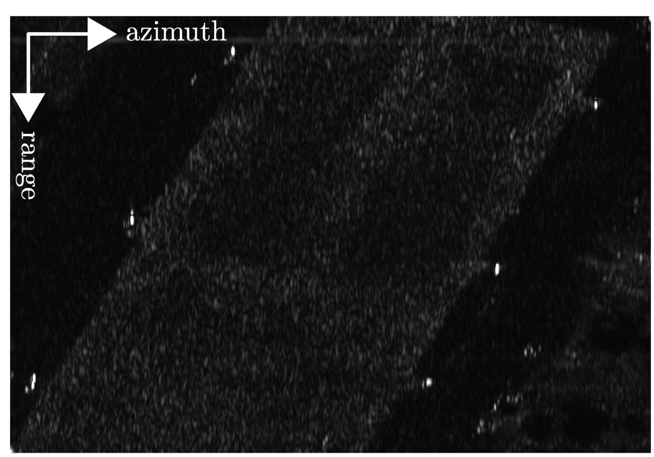

(b)

Fig. 17. Mean intensity map of a relatively flat area in the (a) sliding and (b) staring spotlight modes.

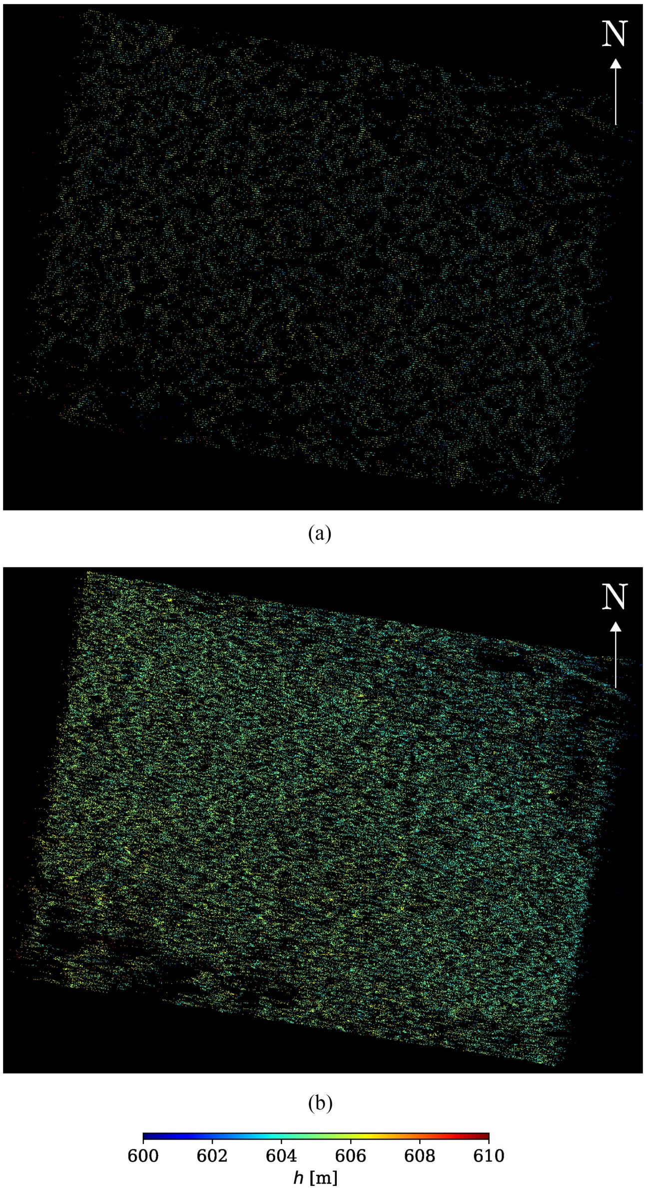

(a)

(b)

Fig. 18. Updated topography h (m) of the area in Fig. 17 with 12 TerraSAR-X images in the (a) sliding and (b) staring spotlight modes, respectively.

Algorithm 1: ADMM-Based Algorithm for Solving (9).

1: **Input:** $\mathbf{A}$, $\mathbf{b}$, ρ
2: **Initialize** $\mathbf{z} \leftarrow \mathbf{0}$, $\mathbf{y} \leftarrow \mathbf{0}$
3: **Until** stopping criterion is satisfied, **Do**
4: $\quad \mathbf{x} \leftarrow (\mathbf{A}^T\mathbf{A})^{-1}\left(\mathbf{A}^T(\mathbf{b}+\mathbf{z}-\frac{1}{\rho}\mathbf{y})\right)$
5: $\quad \mathbf{z} \leftarrow \text{prox}_{\ell_1,1/\rho}(\mathbf{A}\mathbf{x}-\mathbf{b}+\frac{1}{\rho}\mathbf{y})$
6: $\quad \mathbf{y} \leftarrow \mathbf{y}+\mathbf{A}\mathbf{x}-\mathbf{b}-\mathbf{z}$
7: **Output:** $\mathbf{x}$

TABLE II
STATISTICS OF THE POINT CLOUDS IN FIG. 18

	Sliding	Staring	Ratio[a]
Total no. of scatterers	26037	142085	5.46
Scatterer density [million/km^2]	2.47	13.46	5.46

[a]The ratio was calculated by dividing the larger value by the smaller value.

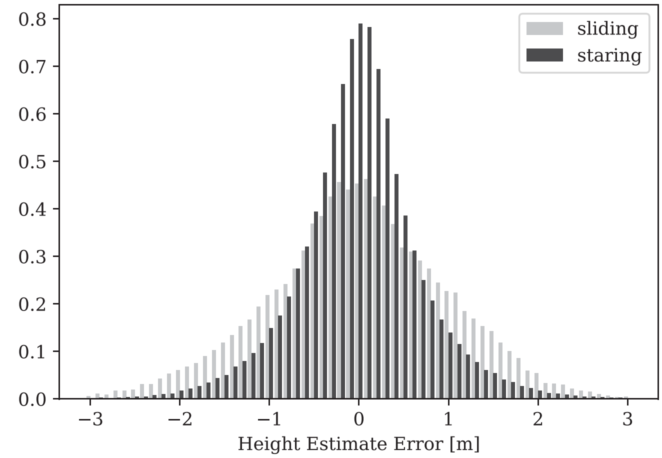

Fig. 19. Normalized histogram of height estimate errors of the point clouds in Fig. 18 relative to a fitted plane.

TABLE III
STATISTICS OF THE HEIGHT ESTIMATE ERRORS IN FIG. 19

	Sliding	Staring	Ratio[a]
Median [m]	0.00	0.00	n.a.
Mean [m]	0.01	0.01	n.a.
Median absolute deviation [m]	0.94	0.54	1.74
Standard deviation [m]	1.12	0.76	1.47

[a]The ratio was calculated by dividing the larger value by the smaller value.

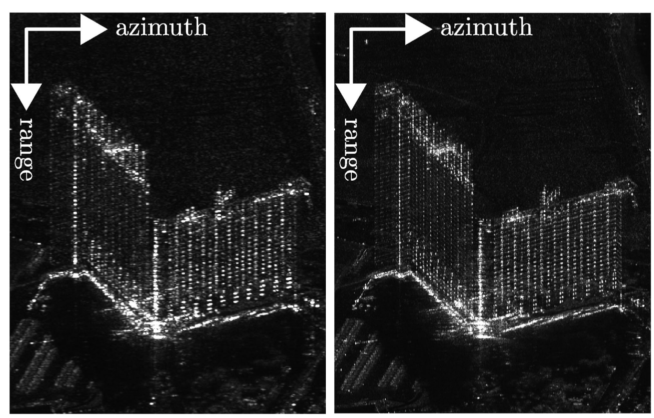

(a) (b)

Fig. 20. Mean intensity map of Hilton Grand Vacations on the Las Vegas Strip and its surroundings in the (a) sliding and (b) staring spotlight modes.

The other area of approximately 0.11 km^2 contains two high-rise buildings and its surroundings. The regular patterns of building facades appear sharper in the staring spotlight mode (see Fig. 20). The reconstructed point clouds are illustrated in Fig. 21 for single- and double-scatterers, respectively. As expected, the staring spotlight mode densified the corresponding point cloud in both single- and double-scatterer cases. In total, the point density in the staring spotlight case is approximately 5.1 times as high (see Table IV). With respect to the ratio of the number of single scatterers to the number of double scatterers, we recorded a slight decrease approximately from 6.9 (sliding) to 6.0 (staring), i.e., no significant difference was observed.

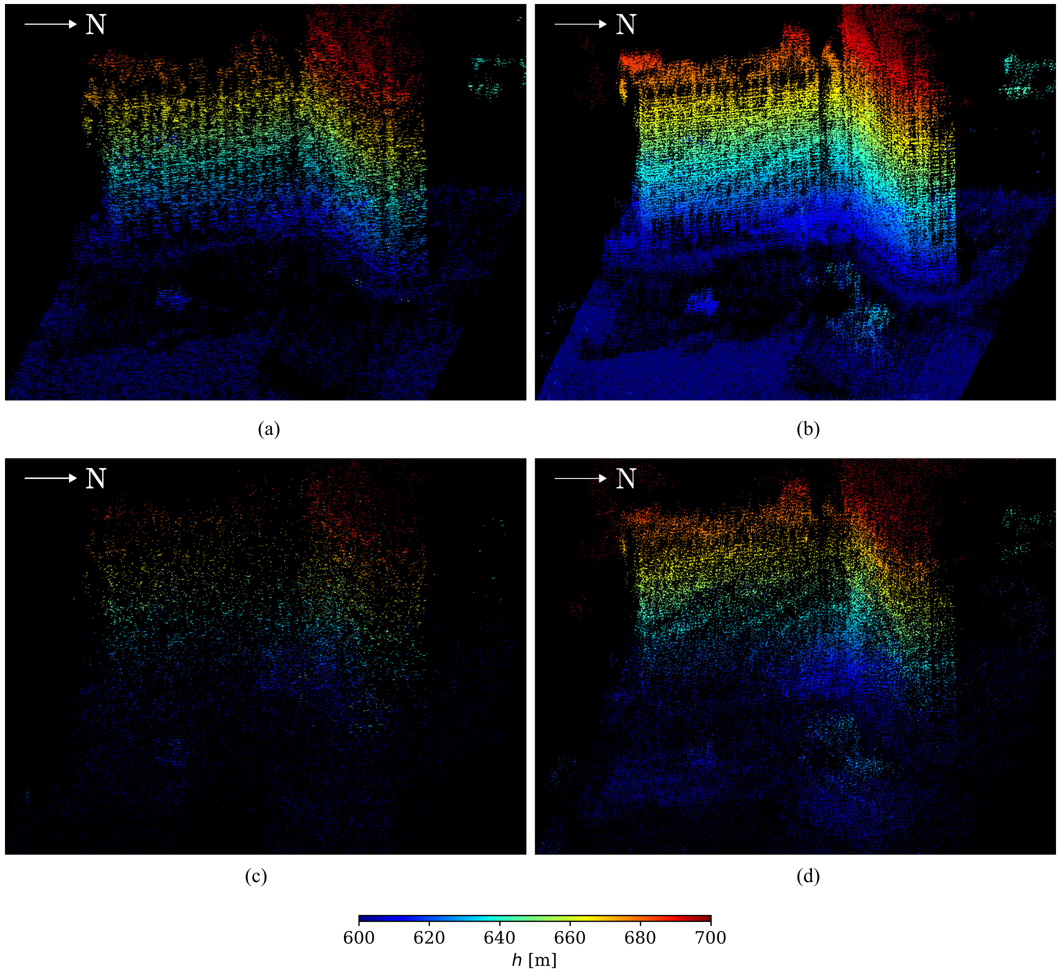

Fig. 21. Updated topography h (m) of the area in Fig. 20 with 12 TerraSAR-X images in the sliding (left column) and staring (right column) spotlight modes, respectively. The upper and lower rows show single and double scatterers, respectively. (a) Single scatterers (sliding). (b) Single scatterers (staring). (c) Double scatterers (sliding). (d) Double scatterers (staring).

TABLE IV
STATISTICS OF THE POINT CLOUDS IN FIG. 21

	Sliding	Staring	Ratio[a]
No. of single scatterers	148646	740656	4.98
No. of double scatterers	21576	124546	5.77
Total no. of scatterers	170222	865202	5.08
Single-to-double-scatterer ratio	6.89	5.95	1.16
Scatterer density [million/km^2]	1.56	7.91	5.08

[a]The ratio was calculated by dividing the larger value by the smaller value.

VI. CONCLUSION

In this paper, we studied the characteristics of the TerraSAR-X staring spotlight mode and its impact on multibaseline InSAR techniques, in particular, the PSI and TomoSAR. The difference in the time-variant Doppler spectra of the sliding and staring spotlight modes was analyzed in concept in order to demonstrate the azimuth resolution versus scene extent tradeoff. The usage of the TerraSAR-X annotation component containing the Doppler centroid in focused image time was proposed to skirt the time conversion issue. The TomoSAR processing chain was revised in order to incorporate sidelobe detection, off-grid correction, and outlier rejection. A first practical demonstration was made with an interferometric stack of 41 images of Washington, DC. The whole scene extent was processed to estimate the topography update of pointlike scatterers and their deformation parameters. Besides, the results of several typical urban areas were visualized and interpreted. A preliminary comparison between the sliding and staring spotlight TomoSAR was drawn in the end with two small interferometric stacks of the City of Las Vegas.

In Section I, we argued that by means of the staring spotlight mode, first, more pointlike targets would be separable in the azimuth–range plane; and, second, each target would have a higher SCR.

As a result, the 4-D point cloud would be not only denser but also more accurate. In this paper, we observed that the density of the *staring* spotlight point cloud is approximately 5.1–5.5 times as high, and the relative height accuracy of the *staring* spotlight point cloud is approximately 1.7 times as high.

Multiple-snapshot TomoSAR approaches, e.g., using an adaptive neighborhood identified within a spatial search window [35], [36] or incorporating additional geospatial information of building footprints [37], could also benefit from the staring spotlight mode. In the former case, the enhanced azimuth resolution

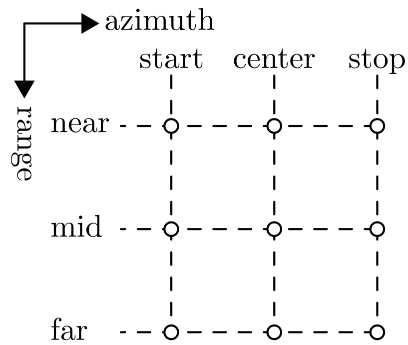

Fig. 22. 3×3 grid of Doppler centroid frequency $f_{\rm DC}$ in focused image time $t_{\rm image}$.

would increase the number of pixels in the homogeneous area; in the latter, the isoheight clusters of a facade to be jointly reconstructed would expand. On the whole, it would lead to a larger number of snapshots and, in turn, to a better estimation accuracy.

Appendix

As previously mentioned in Section II, $f_{\rm DC}$ is provided in $t_{\rm image}$ on a 3×3 grid as a TerraSAR-X annotation component [13]. This grid is defined as the Cartesian product of the sets $\{\text{start}\, t_{\rm image},\ \text{center}\, t_{\rm image},\ \text{stop}\, t_{\rm image}\}$ and $\{\text{near range},\ \text{midrange},\ \text{far range}\}$, as depicted in Fig. 22. This information could be employed to bypass time conversion from $t_{\rm raw}$ to $t_{\rm image}$ and to consider second-order variations of the $f_{\rm DC}$ along a range. Note that this grid is also provided for each burst of any ScanSAR SSC product.

Acknowledgment

TerraSAR-X data were provided by the German Aerospace Center (DLR) under the TerraSAR-X New Modes AO Project LAN2188 and the TanDEM-X Science Phase AO Project NTI_INSA6729. The authors would like to express their gratitude to TerraSAR-X Science Co-ordinator U. Marschalk for her kind support. The authors would also like to thank H. Breit and Dr. T. Fritz for their advice on TerraSAR-X annotation components, N. Adam for his comment on the relation between spatial resolution and the density of double scatterers, S. Montazeri for sharing his experience of sliding spotlight TomoSAR, Dr. M. Lachaise for the discussion about vertical accuracy, A. Parizzi for explaining the principles of sidelobe detection, and the reviewers for their constructive and insightful comments.

References

[1] M. Eineder, N. Adam, R. Bamler, N. Yague-Martinez, and H. Breit, “Spaceborne spotlight SAR interferometry with TerraSAR-X,” *IEEE Trans. Geosci. Remote Sens.*, vol. 47, no. 5, pp. 1524–1535, May 2009.

[2] S. Gernhardt, N. Adam, M. Eineder, and R. Bamler, “Potential of very high resolution SAR for persistent scatterer interferometry in urban areas,” *Ann. GIS*, vol. 16, no. 2, pp. 103–111, 2010.

[3] X. Cong, M. Eineder, and T. Fritz, “Atmospheric delay compensation in differential SAR interferometry for volcanic deformation monitoring-study case: El Hierro,” in *Proc. IEEE Int. Geosci. Remote Sens. Symp.*, 2012, pp. 3887–3890.

[4] X. X. Zhu and R. Bamler, “Very high resolution spaceborne SAR tomography in urban environment,” *IEEE Trans. Geosci. Remote Sens.*, vol. 48, no. 12, pp. 4296–4308, Dec. 2010.

[5] D. Reale, G. Fornaro, A. Pauciullo, X. Zhu, and R. Bamler, “Tomographic imaging and monitoring of buildings with very high resolution SAR data,” *IEEE Geosci. Remote Sens. Lett.*, vol. 8, no. 4, pp. 661–665, Jul. 2011.

[6] M. Bartusch, “HRWS high resolution wide swath: The next national X-band SAR mission,” in *Proc. TerraSAR-X/TanDEM-X Sci. Team Meeting*, DLR, Oberpfaffenhofen, Germany, Oct. 17–20, 2016.

[7] J. Mittermayer, S. Wollstadt, P. Prats-Iraola, and R. Scheiber, “The TerraSAR-X staring spotlight mode concept,” *IEEE Trans. Geosci. Remote Sens.*, vol. 52, no. 6, pp. 3695–3706, Jun. 2014.

[8] P. Prats-Iraola *et al.*, “On the processing of very high resolution spaceborne SAR data,” *IEEE Trans. Geosci. Remote Sens.*, vol. 52, no. 10, pp. 6003–6016, Oct. 2014.

[9] R. Bamler, M. Eineder, N. Adam, X. Zhu, and S. Gernhardt, “Interferometric potential of high resolution spaceborne SAR,” *Photogrammetrie-Fernerkundung-Geoinf.*, vol. 2009, no. 5, pp. 407–419, 2009.

[10] M. Eineder and T. Fritz, “TerraSAR-X basic product specification document,” Tech. Rep. TX-GS-DD-3302, 2013. [Online]. Available: https://sss.terrasar-x.dlr.de/docs/TX-GS-DD-3302.pdf

[11] H. Breit, T. Fritz, U. Balss, M. Lachaise, A. Niedermeier, and M. Vonavka, “TerraSAR-X SAR processing and products,” *IEEE Trans. Geosci. Remote Sens.*, vol. 48, no. 2, pp. 727–740, Feb. 2010.

[12] S. Duque, H. Breit, U. Balss, and A. Parizzi, “Absolute height estimation using a single TerraSAR-X staring spotlight acquisition,” *IEEE Geosci. Remote Sens. Lett.*, vol. 12, no. 8, pp. 1735–1739, Aug. 2015.

[13] T. Fritz and R. Werninghaus, “TerraSAR-X ground segment level 1b product format specification,” Tech. Rep. TX-GS-DD-3307, 2007.

[14] N. Adam, F. R. Gonzalez, A. Parizzi, and R. Brcic, “Wide area persistent scatterer interferometry: Current developments, algorithms and examples,” in *Proc. IEEE Int. Geosci. Remote Sens. Symp.*, 2013, pp. 1857–1860.

[15] F. Rodriguez Gonzalez, N. Adam, A. Parizzi, and R. Brcic, “The integrated wide area processor (IWAP): A processor for wide area persistent scatterer interferometry,” in *Proc. ESA Living Planet Symp.*, 2013, pp. 353–356.

[16] A. Reigber and A. Moreira, “First demonstration of airborne SAR tomography using multibaseline L-band data,” *IEEE Trans. Geosci. Remote Sens.*, vol. 38, no. 5, pp. 2142–2152, Sep. 2000.

[17] F. Gini, F. Lombardini, and M. Montanari, “Layover solution in multibaseline SAR interferometry,” *IEEE Trans. Aerosp. Electron. Syst.*, vol. 38, no. 4, pp. 1344–1356, Oct. 2002.

[18] G. Fornaro, F. Lombardini, and F. Serafino, “Three-dimensional multipass SAR focusing: Experiments with long-term spaceborne data,” *IEEE Trans. Geosci. Remote Sens.*, vol. 43, no. 4, pp. 702–714, Apr. 2005.

[19] F. Lombardini, “Differential tomography: A new framework for SAR interferometry,” *IEEE Trans. Geosci. Remote Sens.*, vol. 43, no. 1, pp. 37–44, Jan. 2005.

[20] G. Fornaro, D. Reale, and F. Serafino, “Four-dimensional SAR imaging for height estimation and monitoring of single and double scatterers,” *IEEE Trans. Geosci. Remote Sens.*, vol. 47, no. 1, pp. 224–237, Jan. 2009.

[21] X. X. Zhu and R. Bamler, “Let’s do the time warp: Multicomponent nonlinear motion estimation in differential SAR tomography,” *IEEE Geosci. Remote Sens. Lett.*, vol. 8, no. 4, pp. 735–739, Jul. 2011.

[22] X. X. Zhu and R. Bamler, “Tomographic SAR inversion by L_1-norm regularization—The compressive sensing approach,” *IEEE Trans. Geosci. Remote Sens.*, vol. 48, no. 10, pp. 3839–3846, Oct. 2010.

[23] A. Budillon, A. Evangelista, and G. Schirinzi, “Three-dimensional SAR focusing from multipass signals using compressive sampling,” *IEEE Trans. Geosci. Remote Sens.*, vol. 49, no. 1, pp. 488–499, Jan. 2011.

[24] Y. T. Yoon, M. Eineder, N. Yague-Martinez, and O. Montenbruck, “TerraSAR-X precise trajectory estimation and quality assessment,” *IEEE Trans. Geosci. Remote Sens.*, vol. 47, no. 6, pp. 1859–1868, Jun. 2009.

[25] X. X. Zhu and R. Bamler, “Super-resolution power and robustness of compressive sensing for spectral estimation with application to spaceborne tomographic SAR,” *IEEE Trans. Geosci. Remote Sens.*, vol. 50, no. 1, pp. 247–258, Jan. 2012.

[26] X. X. Zhu and R. Bamler, “Superresolving SAR tomography for multidimensional imaging of urban areas: Compressive sensing-based TomoSAR inversion,” *IEEE Signal Process. Mag.*, vol. 31, no. 4, pp. 51–58, Jul. 2014.

[27] N. Adam, A. Parizzi, M. Eineder, and M. Crosetto, “Practical persistent scatterer processing validation in the course of the Terrafirma project,” *J. Appl. Geophys.*, vol. 69, no. 1, pp. 59–65, 2009.

[28] R. Iglesias and J. J. Mallorqui, “Side-lobe cancelation in DInSAR pixel selection with SVA,” *IEEE Geosci. Remote Sens. Lett.*, vol. 10, no. 4, pp. 667–671, Jul. 2013.

[29] A. Ferretti, C. Prati, and F. Rocca, “Permanent scatterers in SAR interferometry,” *IEEE Trans. Geosci. Remote Sens.*, vol. 39, no. 1, pp. 8–20, Jan. 2001.

[30] Y. Wang, X. X. Zhu, and R. Bamler, “An efficient tomographic inversion approach for urban mapping using meter resolution SAR image stacks,” *IEEE Geosci. Remote Sens. Lett.*, vol. 11, no. 7, pp. 1250–1254, Jul. 2014.

[31] I. Hajnsek, T. Busche, G. Krieger, M. Zink, and A. Moreira, “Announcement of opportunity: TanDEM-X science phase,” DLR Public Document TD-PD-PL-0032, 2014, no. 10. [Online]. Available: https://tandemx-science.dlr.de/pdfs/TD-PD-PL_0032TanDEM-X_Science_Phase.pdf

[32] S. Boyd and L. Vandenberghe, *Convex Optimization*. Cambridge, U.K.: Cambridge Univ. Press, 2004.

[33] S. Boyd *et al.*, *Distributed Optimization and Statistical Learning via the Alternating Direction Method of Multipliers* (Foundations and Trends® in Machine Learning Series 3). Delft, The Netherlands, 2011, pp. 1–122.

[34] N. Parikh and S. Boyd, *Proximal Algorithms* (Foundations and Trends® in Optimization 3). Delft, The Netherlands, 2014, pp. 127–239.

[35] G. Fornaro, S. Verde, D. Reale, and A. Pauciullo, “CAESAR: An approach based on covariance matrix decomposition to improve multibaseline–multitemporal interferometric SAR processing,” *IEEE Trans. Geosci. Remote Sens.*, vol. 53, no. 4, pp. 2050–2065, Apr. 2015.

[36] M. Schmitt and U. Stilla, “Compressive sensing based layover separation in airborne single-pass multi-baseline InSAR data,” *IEEE Geosci. Remote Sens. Lett.*, vol. 10, no. 2, pp. 313–317, Mar. 2013.

[37] X. X. Zhu, N. Ge, and M. Shahzad, “Joint sparsity in SAR tomography for urban mapping,” *IEEE J. Sel. Topics Signal Process.*, vol. 9, no. 8, pp. 1498–1509, Dec. 2015.

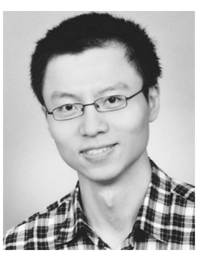

Nan Ge received the Bachelor’s and Master’s degrees in geoenvironmental engineering from TU Clausthal, Clausthal-Zellerfeld, Germany, in 2007 and 2010, respectively. Since 2013, he has been working toward the Doctoral degree by developing advanced tomographic techniques for very high resolution SAR systems at the Remote Sensing Technology Institute, German Aerospace Center (DLR), Wessling, Germany.

Fernando Rodriguez Gonzalez received the Ingeniero degree in telecommunications engineering from the Universidad Politécnica de Madrid, Madrid, Spain, and the Diplôme de l’École Polytechnique degree from the École Polytechnique, Palaiseau, France, in 2009.

From 2009 to 2010, he was the Chair of Remote Sensing Technology, Technische Universität München, Munich, Germany. In 2010, he was with the SAR Signal Processing Department, Remote Sensing Technology Institute, German Aerospace Center (DLR), Wessling, Germany. He was involved with the development of the operational interferometric processor of the TanDEM-X mission. His research interests include InSAR, PSI, and SAR stereo radargrammetry.

Yuanyuan Wang (S’10–M’14) received the B.Eng. (Hons.) degree in electrical engineering from The Hong Kong Polytechnic University, Hong Kong, in 2008, and the M.Sc. degree as well as the Dr.-Ing. degree in signal processing from Technical University of Munich (TUM), Munich, Germany, in 2010 and 2015, respectively.

In June and July of 2014, he was a Guest Scientist at the Institute of Visual Computing, ETH Zurich, Zurich, Switzerland. He is currently with Signal Processing in Earth Observation, TUM, working on coordination and algorithm development of the European project So2Sat: Big Data for 4D Global Urban Mapping—10ˆ16 Bytes from Social Media to Earth Observation Satellites (So2Sat, www.so2sat.eu). His research interests include optimal and robust parameters estimation in multibaseline InSAR techniques, multisensor fusion algorithms of InSAR and optical data, nonlinear optimization for complex numbers, and the applications of these techniques in urban and volcanic areas.

Dr. Wang is a Reviewer for several remote sensing journals, as well as a Reviewer for the European Research Council and the French National Research Agency. In 2016, he was one of the best reviewers for IEEE TRANSACTIONS ON GEOSCIENCE AND REMOTE SENSING.

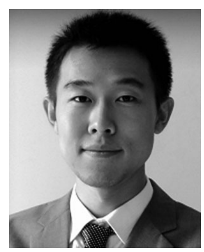

Yilei Shi (M’18) received the Diploma degree in mechanical engineering from the Technical University of Munich (TUM), Munich, Germany, in 2010.

He is currently a Research Associate with the Chair of Remote Sensing Technology, TUM, working on the European project So2Sat: Big Data for 4D Global Urban Mapping—10ˆ16 Bytes from Social Media to Earth Observation Satellites (So2Sat, www.so2sat.eu) and developing algorithms for global 3-D urban modeling. His research interests include fast solver and parallel computing for large-scale problems, advanced methods on SAR and InSAR processing, machine learning and deep learning for a variety of data sources, such as SAR, optical images, medical images, etc., and PDE-related numerical modeling and computing.

Xiao Xiang Zhu (S’10–M’12–SM’14) received the M.Sc., Dr.-Ing. degrees, and the “Habilitation” in the field of signal processing from the Technical University of Munich (TUM), Munich, Germany, in 2008, 2011, and 2013, respectively.

She is currently the Professor for Signal Processing in Earth Observation, TUM, and also with the German Aerospace Center (DLR), Wessling, Germany. She is the Head of the “EO Data Science” Department, Earth Observation Center, DLR, and the Head of the Helmholtz Young Investigator Group “SiPEO” at DLR and TUM. She was a Guest Scientist or Visiting Professor with the Italian National Research Council (CNR-IREA), Naples, Italy, Fudan University, Shanghai, China, the University of Tokyo, Tokyo, Japan, and the University of California, Los Angeles, CA, USA, in 2009, 2014, 2015, and 2016, respectively. Her research interests include remote sensing and earth observation, signal processing, machine learning and data science, with a special application focus on global urban mapping.

Dr. Zhu is a member of the Young Academy (Junge Akademie/Junges Kolleg) at the Berlin-Brandenburg Academy of Sciences and Humanities, Berlin, Germany, the German National Academy of Sciences Leopoldina, Schweinfurt, Germany, and the Bavarian Academy of Sciences and Humanities, Munich, Germany. She is an Associate Editor for IEEE TRANSACTIONS ON GEOSCIENCE AND REMOTE SENSING.